China Ocean Eng., 2019, Vol. 33, No. 1, P. 1–13
DOI: 10.1007/s13344-019-0001-0, ISSN 0890-5487
http://www.chinaoceanengin.cn/ E-mail: coe@nhri.cn

Study on Rigid-Flexible Coupling Effects of Floating Offshore Wind Turbines

CHEN Jia-hao[a, c], HU Zhi-qiang[b, *], LIU Ge-liang[a], WAN De-cheng[a, c]

[a]State Key Laboratory of Ocean Engineering, Shanghai Jiao Tong University, Shanghai 200240, China

[b]School of Engineering, Newcastle University, Newcastle upon Tyne, NE1 7RU, UK

[c]Collaborative Innovation Center for Advanced Ship and Deep-Sea Exploration, Shanghai Jiao Tong University, Shanghai 200240, China

Received April 29, 2018; revised September 10, 2018; accepted November 15, 2018

Abstract

In order to account for rigid-flexible coupling effects of floating offshore wind turbines, a nonlinear rigid-flexible coupled dynamic model is proposed in this paper. The proposed nonlinear coupled model takes the higher-order axial displacements into account, which are usually neglected in the conventional linear dynamic model. Subsequently, investigations on the dynamic differences between the proposed nonlinear dynamic model and the linear one are conducted. The results demonstrate that the stiffness of the turbine blades in the proposed nonlinear dynamic model increases with larger overall motions but that in the linear dynamic model declines with larger overall motions. Deformation of the blades in the nonlinear dynamic model is more reasonable than that in the linear model as well. Additionally, more distinct coupling effects are observed in the proposed nonlinear model than those in the linear model. Finally, it shows that the aerodynamic loads, the structural loads and global dynamic responses of floating offshore wind turbines using the nonlinear dynamic model are slightly smaller than those using the linear dynamic model. In summary, compared with the conventional linear dynamic model, the proposed nonlinear coupling dynamic model is a higher-order dynamic model in consideration of the rigid-flexible coupling effects of floating offshore wind turbines, and accord more perfectly with the engineering facts.

Key words: floating offshore wind turbine, dynamic stiffening effect, nonlinear coupled dynamic model, DARwind

Citation: Chen, J. H., Hu, Z. Q., Liu, G. L., Wan, D. C., 2019. Study on rigid-flexible coupling effects of floating offshore wind turbines. China Ocean Eng., 33(1): 1–13, doi: 10.1007/s13344-019-0001-0

1 Introduction

In recent years, floating offshore wind turbines (FOWTs) have been receiving increasing attention due to their prominent advantages, such as steadier and stronger wind available resources, lower operational noise, reduced visual pollution and fewer space limitations (Karimirad et al., 2011; Bachynski and Moan, 2012; Pérez-Collazo et al., 2015; Ma et al., 2015). FOWTs are complex rigid-flexible coupled multi-body systems (Namik and Stol, 2010; Wang and Sweetman, 2013; Nejad et al., 2015). Moreover, because the slender blades of an FOWT system typically work at a high rotational speed and are influenced by the motions of the floating platform, rigid-flexible coupled dynamic responses of FOWT systems are more complicated than those of the fixed bottom wind turbines.

Rigid-flexible coupled multi-body dynamics have received considerable attentions during the development of modern high-speed airplanes (Shabana, 1997; Bauchau, 2011). In the 1970s, Winfrey (1971) proposed the "kineto-elastodynamics" (KED) method to model the dynamic behaviour of rigid-flexible coupled multi-body systems. In this method, the system is first modelled as a rigid multi-body system to calculate the motion and inertia forces on the system. Second, the inertia and external forces are applied to the flexible components of the system to calculate the deformation and the motion of the flexible components. The KED method is a decoupled method with the linear structural dynamics and kinematics of a rigid multi-body system. Hence, the coupling effects between the flexible bodies and the large overall motions from rigid bodies were not considered. Likins (1972) proposed the "hybrid-coordinate dynamic model" to describe the dynamic behaviour of rigid-flexible coupled multi-body systems. In this method, the flexible deformation is described with respect to the local body-fixed frames; then, the configuration of the system can be described as a superposition of the motions of these

Foundation item: This work was financially supported by the Ministry of Industry and Information Technology of China (Grant No. [2016]546).
*Corresponding author. E-mail: Zhiqiang.Hu@newcastle.ac.uk

body-fixed frames and the flexible deformation with respect to these body-fixed frames. This method accounts for the coupling effects between the flexible bodies and the large overall motions of the rigid bodies to some extent. However, the hybrid-coordinate dynamic model above is a linear method in fact, and certain higher-order quantities are neglected, which may cause some inaccurate dynamic results under large overall motions. Kane et al. (1989) studied the dynamic behaviour of a cantilever beam attached to a moving boundary and found that the deformation of the beam in the linear hybrid-coordinate dynamic model would tend toward infinity with the increasing rotational speed, which contradicted the reality that the stiffness of a cantilever beam should increase with the increasing rotational speed. Kane firstly proposed "dynamic stiffening" to describe this phenomenon. Other experiments also demonstrated significant coupling effects between the flexible bodies and the large overall motions (Lee et al., 2001; Santos et al., 2004). Since then, coupling effects and the defects of the linear dynamic model have attracted considerable attention. Although several researchers have corrected the linear dynamic model to successfully detect dynamic stiffening effects in a rigid-flexible coupled multi-body system using different methods (Banerjee and Dickens, 1990; Liu and Liew, 1994; Mayo et al., 1995; Sharf, 1995), there is still no widespread consensus regarding the essence of these coupling effects. The omission of the higher-order strain-displacement relationship in the linear dynamic model could be the reason for the failure to model dynamic stiffening effects in a rigid-flexible coupled multi-body system (Mayo et al., 1995). After investigating the dynamic characteristics of a cantilever beam attached to a moving base, Liu and Hong (2003, 2004) found that the inaccuracy in the linear dynamic model is caused by the omission of the axial foreshortening displacement induced by the lateral displacements when undergoing large overall motions.

In the wind energy field, researchers (Lee et al., 2002; Santos et al., 2004; Larsen and Nielsen, 2006) have found that these coupling effects are important for the blades of fixed-bottom wind turbines as well. Compared with fixed-bottom wind turbine systems, FOWTs are the relatively new concept and their blades are slenderer and the six-degree-of-freedom (DOF) motion of the floating platform usually gives rise to large overall motions of the blades. Thus, nonlinear rigid-flexible coupling effects in FOWTs are more distinct, but the related researches are scarce.

The purpose of this study is to propose an appropriate rigid-flexible coupling dynamic model and to investigate the coupling rigid-flexible effects of the floating wind turbine system. Hence, the work of the paper includes:

(1) Deducing a nonlinear coupling dynamic model applied to the FOWTs modelling.

(2) Comparing dynamic differences between the proposed nonlinear dynamic model and the linear one in an FOWT system.

(3) Investigating rigid-flexible coupling effects of an FOWT system.

In view of the fact that the movement of the foundation of the tower is relatively small and the deformation of the shaft is negligible, thus, the tower is modeled as a linear model and the shaft is modeled as a rigid body. In other words, the nonlinear rigid-flexible modeling is only applied to the blades. This paper makes contribution for a better understanding of the rigid-flexible coupled dynamic effects of an FOWT system and hopes to raise awareness of this issue in the FOWTs research community.

2 Theories and methodology

In this section, the theories on the linear dynamic model and the proposed nonlinear coupled dynamic model are introduced in details. First, the fundamental kinematic method is presented. Subsequently, the dynamic governing equation for a three-dimensional flexible beam undergoing large overall motions is deduced to compare the essential distinction between the linear dynamic model and the nonlinear coupled dynamic model.

2.1 Kinematics description

The "floating frame of reference formulation" method (Nada et al., 2010; Nowakowski et al., 2012; Held et al., 2016) is used to describe the kinematics of an FOWT system. In this method, there are two sets of coordinate frames. One is the global reference frame (RF), which describes the location and the orientation of the bodies, and the other is the local elastic body-fixed frame (BF), which describes the elastic deformation of flexible bodies. This method is schematically illustrated in Fig. 1, where $\underline{e}^0$ is the global reference coordinate frame (RF) and $\underline{e}^{\mathrm{b}}$ is the local body-fixed coordinate frame (BF).

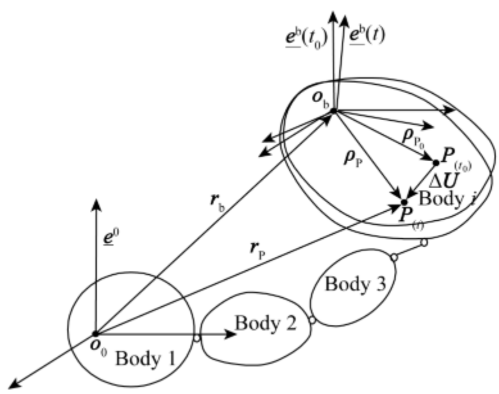

Fig. 1. Floating reference frame.

The position of an arbitrary point P with respect to the body-fixed frame $\underline{e}^{\mathrm{b}}(t)$ in the undeformed state is denoted as $\boldsymbol{\rho}_{\mathrm{P}_0}$. The deformation of this point is defined as $\Delta\boldsymbol{U}$. Hence, the position vector of Point P after deformation with respect to $\underline{e}^{\mathrm{b}}(t)$ is written as follows:

$$\boldsymbol{\rho}_{\mathrm{P}} = \boldsymbol{\rho}_{\mathrm{P}_0} + \Delta\boldsymbol{U}. \tag{1}$$

The position vector of Point P after deformation with respect to the global reference frame $\underline{e}^0$ is written as follows:

$$\boldsymbol{r}_{\mathrm{P}} = \boldsymbol{r}_{\mathrm{b}} + \boldsymbol{\rho}_{\mathrm{P}}. \tag{2}$$

Substituting Eq. (1) into Eq. (2) yields:

$$\boldsymbol{r}_{\mathrm{P}} = \boldsymbol{r}_{\mathrm{b}} + \boldsymbol{\rho}_{\mathrm{P}_0} + \Delta\boldsymbol{U}. \tag{3}$$

According to Eq. (3), the velocity vector of Point P is the first derivative of the position vector $\boldsymbol{r}_{\mathrm{P}}$, written as follows:

$$\dot{\boldsymbol{r}}_{\mathrm{P}} = \dot{\boldsymbol{r}}_{\mathrm{b}} + \boldsymbol{\omega}\times\left(\boldsymbol{\rho}_{\mathrm{P}_0} + \Delta\boldsymbol{U}\right) + \Delta\underline{\dot{\boldsymbol{U}}}, \tag{4}$$

where $\boldsymbol{\omega}$ is the instantaneous angular velocity vector of the body with respect to $\underline{e}^0$, $\Delta\underline{\dot{\boldsymbol{U}}}$ denotes the first-order derivative of the deformation versus time with respect to the local body-fixed frame $\underline{e}^{\mathrm{b}}(t)$ and the symbol $\times$ indicates the cross product.

Based on Eq. (4), the acceleration vector of Point P with respect to the global reference frame $\underline{e}^0$ is written as follows:

$$\begin{aligned}\ddot{\boldsymbol{r}}_{\mathrm{P}} =& \ddot{\boldsymbol{r}}_{\mathrm{b}} + \dot{\boldsymbol{\omega}}\times\left(\boldsymbol{\rho}_{\mathrm{P}_0} + \Delta\boldsymbol{U}\right) + 2\boldsymbol{\omega}\times\Delta\underline{\dot{\boldsymbol{U}}} + \boldsymbol{\omega}\times\\ &\left[\boldsymbol{\omega}\times\left(\boldsymbol{\rho}_{\mathrm{P}_0} + \Delta\boldsymbol{U}\right)\right] + \Delta\underline{\ddot{\boldsymbol{U}}},\end{aligned} \tag{5}$$

where $\Delta\underline{\ddot{\boldsymbol{U}}}$ denotes the second-order derivative of the deformation versus time with respect to the local body-fixed frame $\underline{e}^{\mathrm{b}}(t)$.

In order to describe the deformation $\Delta\boldsymbol{U}$ in a rigid-flexible coupled multi-body system, Likins (1972) proposed the linear hybrid-coordinate dynamic model. In this method, the kinematic relationship between rigid and flexible bodies is described by the floating frame of the reference formulation described above, and the flexible deformation is based on the small deformation assumption, in which the geometrically nonlinear quantities are neglected to linearize the deformation field. However, the neglected certain geometrically nonlinear quantities in this linear dynamic model may be significant for a rigid-flexible coupled multi-body system undergoing large overall motions. Therefore, the study in this paper proposes a nonlinear dynamic model in consideration of these geometrically nonlinear high-order quantities in a rigid-flexible coupled multi-body system. In the following sections, the linear dynamic model presented above is denoted "L-model" (low-order model), and the proposed nonlinear dynamic model is denoted "H-model" (higher-order model).

2.2 Dynamic governing equations

In this subsection, the dynamic governing equation for a three-dimensional flexible beam with large overall motions is deduced. In addition, the essential difference between the linear dynamic model and the proposed nonlinear dynamic model will be discussed.

Because the blades of an FOWT are slender and attached to a hub, the blades can be modeled as an Euler–Bernoulli cantilever beam attached to a movable rigid boundary. For simplicity, in the following sections, the cantilever beam is homogeneous and isotropic, and the centroid axis of the cross section along the beam is also coincident. A three-dimensional Euler–Bernoulli cantilever beam with large overall motions is shown in Fig. 2, where $O_{\mathrm{b}} - {}^{\mathrm{b}}e_x{}^{\mathrm{b}}e_y{}^{\mathrm{b}}e_z$ is the local body-fixed frame of the cantilever beam. The hub rotates at an angular velocity ω. Point k_0 is at the position x along the undeformed neutral axis of the beam. After deformation, Point k_0 moves to a new position k. $\boldsymbol{U}_k$ is the deformation vector of the point and can be written as:

$$\boldsymbol{U}_k = \begin{bmatrix} u_{x0} \\ u_{y0} \\ u_{z0} \end{bmatrix} \tag{6}$$

where u_{x0}, u_{y0} and u_{z0} are the coordinate components of deformation $\boldsymbol{U}_k$ along the coordinate axes ${}^{\mathrm{b}}e_x$, ${}^{\mathrm{b}}e_y$ and ${}^{\mathrm{b}}e_z$, respectively.

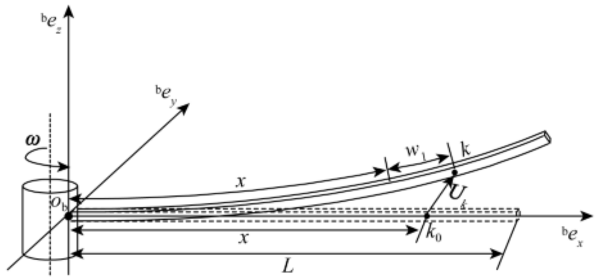

Fig. 2. Three-dimensional cantilever beam with large overall motions.

Assuming that the length of a differential element at the position x is dx before deformation, the stretch of this element along the neutral axis after deformation can be written as:

$$\mathrm{d}s = \sqrt{\left(1+\frac{\mathrm{d}u_{x0}}{\mathrm{d}x}\right)^2 + \left(\frac{\mathrm{d}u_{y0}}{\mathrm{d}x}\right)^2 + \left(\frac{\mathrm{d}u_{z0}}{\mathrm{d}x}\right)^2}\cdot\mathrm{d}x \tag{7}$$

Hence, the axial normal strain ε_0 is:

$$\varepsilon_0 = \frac{\mathrm{d}s - \mathrm{d}x}{\mathrm{d}x}. \tag{8}$$

Substituting Eq. (7) into Eq. (8), and then expanding the equation by the Taylor expansion yields:

$$\varepsilon_0 \approx \frac{\mathrm{d}u_{x0}}{\mathrm{d}x} + \frac{1}{2}\left[\left(\frac{\mathrm{d}u_{y0}}{\mathrm{d}x}\right)^2 + \left(\frac{\mathrm{d}u_{z0}}{\mathrm{d}x}\right)^2\right]. \tag{9}$$

According to Eq. (9), the stretch of the beam at Point k can be obtained by an integral from zero to the position x:

$$w_1 = \int_0^x \varepsilon_0 \mathrm{d}x = u_{x0} + \frac{1}{2}\int_0^x \left[\left(\frac{\mathrm{d}u_{y0}}{\mathrm{d}x}\right)^2 + \left(\frac{\mathrm{d}u_{z0}}{\mathrm{d}x}\right)^2\right]\mathrm{d}x. \tag{10}$$

Let

$$w_{\rm g}=-\frac{1}{2}\int_0^x\left[\left(\frac{{\rm d}u_{y0}}{{\rm d}x}\right)^2+\left(\frac{{\rm d}u_{z0}}{{\rm d}x}\right)^2\right]{\rm d}x, \tag{11}$$

and thus,

$$u_{x0}=w_1+w_{\rm g}. \tag{12}$$

Eq. (11) indicates that $w_{\rm g}$ is an axial foreshortening displacement along ${}^{\rm b}e_x$ caused by the coupling effects from the lateral displacements u_{y0} and u_{z0}. Considering this foreshortening displacement or not is the essential difference between the linear dynamic model (L-model) and the proposed nonlinear dynamic model (H-model).

For an arbitrary point in the cross-section of a beam, an additional axial displacement along ${}^{\rm b}e_x$ caused by the cross-sectional rotation effect can be approximated as follows:

$$w_{\rm r}\approx -y\frac{\partial w_2}{\partial x}-z\frac{\partial w_3}{\partial x}. \tag{13}$$

Hence, the deformation of an arbitrary point in the cross-section of an Euler-Bernoulli cantilever beam is written as:

$$\boldsymbol{U}=\begin{bmatrix}u_{x0}\\u_{y0}\\u_{z0}\end{bmatrix}=\begin{bmatrix}w_1+w_{\rm g}+w_{\rm r}\\w_2\\w_3\end{bmatrix}, \tag{14}$$

where w_1 is the stretch along the neutral axis, and w_2 and w_3 are the lateral displacements induced by the bending deflections with respect to the body-fixed frame. $w_{\rm g}$ and $w_{\rm r}$ are the lateral-displacement-induced axial displacement and section-rotation-induced axial displacement, respectively.

By substituting Eqs. (11) and (13) into Eq. (14), the x-axis displacement u_{x0} (see Fig. 2) can be written as:

$$u_{x0}=w_1+w_{\rm g}+w_{\rm r}=w_1-\frac{1}{2}\int_0^x\left[\left(\frac{{\rm d}u_{y0}}{{\rm d}x}\right)^2+\left(\frac{{\rm d}u_{z0}}{{\rm d}x}\right)^2\right]{\rm d}x-y\frac{\partial w_2}{\partial x}-z\frac{\partial w_3}{\partial x}. \tag{15}$$

According to Eq. (9) and Eq. (15), the strain power of the beam can be approximated as follows:

$$\dot{V}=\int_0^L\int_A\sigma{\rm d}A\dot{\varepsilon}{\rm d}x\approx\int_0^L EA\left(\frac{\partial w_1}{\partial x}\right)\left(\frac{\partial w_1}{\partial x\partial t}\right){\rm d}x+\int_0^L EI_{zz}\left(\frac{\partial^2 w_2}{\partial x^2}\right)\left(\frac{\partial^2 w_2}{\partial x^2\partial t}\right){\rm d}x+\int_0^L EI_{yy}\left(\frac{\partial^2 w_3}{\partial x^2}\right)\left(\frac{\partial^2 w_3}{\partial x^2\partial t}\right){\rm d}x, \tag{16}$$

where $I_{zz}=\int_A y^2{\rm d}A$ and $I_{yy}=\int_A z^2{\rm d}A$ are the central principal second moments of the area with respect to the z-axis and y-axis, respectively; E is Young's modulus and A is the cross-sectional area.

In this paper, the modal superposition method (Andreaus et al., 2016) is used to disperse the beam model. Thus, axial and lateral deformation can be dispersed as:

$$w_1=\sum_{i=1}^n\phi_{xi}q_{xi}=\boldsymbol{\Phi}_x^{\rm T}\boldsymbol{q}_x=\boldsymbol{q}_x^{\rm T}\boldsymbol{\Phi}_x; \tag{17}$$

$$w_2=\sum_{i=1}^n\phi_{yi}q_{yi}=\boldsymbol{\Phi}_y^{\rm T}\boldsymbol{q}_y=\boldsymbol{q}_y^{\rm T}\boldsymbol{\Phi}_y; \tag{18}$$

$$w_3=\sum_{i=1}^n\phi_{zi}q_{zi}=\boldsymbol{\Phi}_z^{\rm T}\boldsymbol{q}_z=\boldsymbol{q}_z^{\rm T}\boldsymbol{\Phi}_z, \tag{19}$$

where ϕ_{xi}, ϕ_{yi} and ϕ_{zi} are the i-th spatial shape functions and q_{xi}, q_{yi} and q_{zi} are the i-th generalized coordinates with respect to the coordinate axes ${}^{\rm b}e_x$, ${}^{\rm b}e_y$ and ${}^{\rm b}e_z$ of the local body-fixed frame, respectively. A cantilevered boundary condition is used for the beam model, in other words, the base of the beam does not experience any deflection $w(0)=0$, the derivative of the deflection function at that point is zero $w'(0)=0$, there is no bending moment at the free end $w''(L)=0$, and there is no shearing force acting at the free end $w'''(L)=0$.

In regard to blades mode order, Øye (1996) found that the first 3 or 4 eigenmodes (2 flapwise eigenmodes, 1 or 2 edgewise eigenmodes) used for a wind turbine are in good agreement with the measurements. Thus, the first 3 eigenmodes (2 flapwise eigenmodes and 1 edgewise eigenmode) are used to disperse the blades in the subsequent tests. Spatial shape functions for the blades are approximated as 6th-order polynomials calculated by the preprocessor Mode (Marshall, 2002), as shown in Fig. 3.

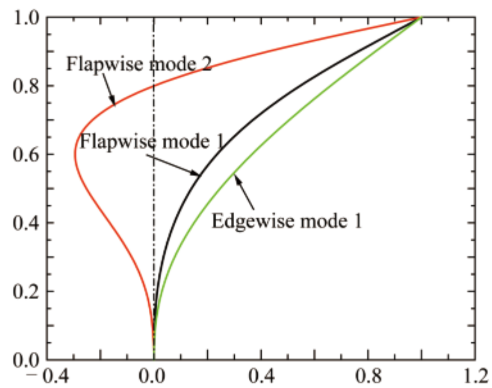

Fig. 3. Spatial shape functions of the blades.

According to Eq. (14), the deformation of an arbitrary point in the cross-section and its first and second derivatives are written as follows:

$$\boldsymbol{U}=\left(\boldsymbol{\Phi}+\frac{1}{2}\boldsymbol{A}_Q^{\rm T}\boldsymbol{H}+\boldsymbol{R}\right)\boldsymbol{Q}; \tag{20}$$

$$\underline{\dot{\boldsymbol{U}}}=\left(\boldsymbol{\Phi}+\boldsymbol{A}_Q^{\rm T}\boldsymbol{H}+\boldsymbol{R}\right)\dot{\boldsymbol{Q}}; \tag{21}$$

$$\underline{\ddot{\boldsymbol{U}}}=\left(\boldsymbol{\Phi}+\boldsymbol{A}_Q^{\rm T}\boldsymbol{H}+\boldsymbol{R}\right)\ddot{\boldsymbol{Q}}+\dot{\boldsymbol{A}}_Q^{\rm T}\boldsymbol{H}\dot{\boldsymbol{Q}}, \tag{22}$$

where

Spatial shape functions matrix:

$$\boldsymbol{\Phi}=\begin{bmatrix}\boldsymbol{\Phi}_x^{\rm T}&0&0\\0&\boldsymbol{\Phi}_y^{\rm T}&0\\0&0&\boldsymbol{\Phi}_z^{\rm T}\end{bmatrix},\begin{cases}\boldsymbol{\Phi}_x=\begin{bmatrix}\phi_{x1}&\phi_{x2}&\cdots&\phi_{xn}\end{bmatrix}\\\boldsymbol{\Phi}_y=\begin{bmatrix}\phi_{y1}&\phi_{y2}&\cdots&\phi_{yn}\end{bmatrix}\\\boldsymbol{\Phi}_z=\begin{bmatrix}\phi_{z1}&\phi_{z2}&\cdots&\phi_{zn}\end{bmatrix}\end{cases} \tag{23}$$

Generalized coordinate matrix:

$$\boldsymbol{Q}=\begin{bmatrix}\boldsymbol{q}_x\\ \boldsymbol{q}_y\\ \boldsymbol{q}_z\end{bmatrix},\begin{cases}\boldsymbol{q}_x=[\ q_{x1}\quad q_{x2}\quad\cdots\quad q_{xn}\ ]\\ \boldsymbol{q}_y=[\ q_{y1}\quad q_{y2}\quad\cdots\quad q_{yn}\ ]\\ \boldsymbol{q}_z=[\ q_{z1}\quad q_{z2}\quad\cdots\quad q_{zn}\ ]\end{cases}\tag{24}$$

$$A_Q=[\ \boldsymbol{Q}\quad \boldsymbol{0}\quad \boldsymbol{0}\ ]\tag{25}$$

Cross-sectional rotation effect matrix:

$$\boldsymbol{R}=\begin{bmatrix}0 & -y\left(\dfrac{\partial\phi_y}{\partial x}\right)^{\mathrm{T}} & -z\left(\dfrac{\partial\phi_z}{\partial x}\right)^{\mathrm{T}}\\ 0 & 0 & 0\\ 0 & 0 & 0\end{bmatrix}\tag{26}$$

Nonlinear coupling effect matrix:

$$\boldsymbol{H}=\begin{bmatrix}0&0&0\\0&\boldsymbol{H}_y&0\\0&0&\boldsymbol{H}_z\end{bmatrix};$$

$$\boldsymbol{H}_y=-\int_0^x\left(\frac{\partial\phi_y}{\partial x}\right)\cdot\left(\frac{\partial\phi_y}{\partial x}\right)^{\mathrm{T}}\mathrm{d}x;$$

$$\boldsymbol{H}_z=-\int_0^x\left(\frac{\partial\phi_z}{\partial x}\right)\cdot\left(\frac{\partial\phi_z}{\partial x}\right)^{\mathrm{T}}\mathrm{d}x.\tag{27}$$

Variational forms of the above terms are rewritten as follows:

$$\delta\underline{\dot{\boldsymbol{U}}}=\left(\boldsymbol{\Phi}+\boldsymbol{R}+\boldsymbol{A}_Q^{\mathrm{T}}\boldsymbol{H}\right)\cdot\delta\dot{\boldsymbol{Q}};\tag{28}$$

$$\delta\underline{\ddot{\boldsymbol{U}}}=\left(\boldsymbol{\Phi}+\boldsymbol{R}+\boldsymbol{A}_Q^{\mathrm{T}}\boldsymbol{H}\right)\cdot\delta\ddot{\boldsymbol{Q}}+\dot{\boldsymbol{A}}_Q^{\mathrm{T}}\boldsymbol{H}\cdot\delta\dot{\boldsymbol{Q}}.\tag{29}$$

From Eq. (4), the velocity of an arbitrary point in the cross section in the variational form is:

$$\delta\dot{\boldsymbol{r}}=\delta\dot{\boldsymbol{r}}_{\mathrm{b}}-\left(\tilde{\boldsymbol{\rho}}_{P_0}+\tilde{\boldsymbol{U}}\right)\cdot\delta\boldsymbol{\omega}+\left(\boldsymbol{\Phi}+\boldsymbol{R}+\boldsymbol{A}_Q^{\mathrm{T}}\boldsymbol{H}\right)\cdot\delta\dot{\boldsymbol{Q}}.\tag{30}$$

From Eq. (16), the virtual strain power of the beam is written as follows:

$$\delta\dot{\boldsymbol{V}}=\delta\dot{\boldsymbol{Q}}^{\mathrm{T}}\boldsymbol{K}_0\boldsymbol{Q},\tag{31}$$

where

Constant stiffness matrix:

$$\boldsymbol{K}_0=\begin{bmatrix}\boldsymbol{K}_x&0&0\\0&\boldsymbol{K}_y&0\\0&0&\boldsymbol{K}_z\end{bmatrix},$$

$$\begin{cases}\boldsymbol{K}_x=\displaystyle\int_0^L EA\left(\frac{\partial\phi_x}{\partial x}\right)\left(\frac{\partial\phi_x}{\partial x}\right)^{\mathrm{T}}\mathrm{d}x\\ \boldsymbol{K}_y=\displaystyle\int_0^L EI_{zz}\left(\frac{\partial^2\phi_y}{\partial x^2}\right)\left(\frac{\partial^2\phi_y}{\partial x^2}\right)^{\mathrm{T}}\mathrm{d}x\\ \boldsymbol{K}_z=\displaystyle\int_0^L EI_{yy}\left(\frac{\partial^2\phi_z}{\partial x^2}\right)\left(\frac{\partial^2\phi_z}{\partial x^2}\right)^{\mathrm{T}}\mathrm{d}x\end{cases}\tag{32}$$

Based on Jourdain's variational principle (Jourdain, 1909; Wang and Pao, 2003), the dynamic equation for the flexible cantilever beam with a movable boundary can be written as:

$$\delta\dot{\boldsymbol{W}}-\int_\Omega\rho\delta\dot{\boldsymbol{r}}^{\mathrm{T}}\ddot{\boldsymbol{r}}\mathrm{d}\Omega-\delta\dot{\boldsymbol{V}}=0,\tag{33}$$

where $\delta\dot{\boldsymbol{W}}$ is the power of the virtual active forces. For simplicity in the following analysis, we assume that the beam vibrates without any active force ($\delta\dot{\boldsymbol{W}}=0$), and the beam performs a specified motion; in other words, we can let the variation $\delta\dot{\boldsymbol{r}}_{\mathrm{b}}=0$ and $\delta\boldsymbol{\omega}=0$. For a slender beam (e.g., offshore wind turbine blades), the transverse size is far smaller than the axial size; thus, additional axial displacements caused by the cross-sectional rotation effect can be neglected, $\boldsymbol{R}=0$. Substituting Eqs. (5), (30) and (31) into Eq. (33), we can obtain the dynamic governing equation of a three-dimensional flexible beam with large overall motions:

$$\delta\dot{\boldsymbol{Q}}^{\mathrm{T}}\left\{\int_\Omega\rho\left(\boldsymbol{\Phi}^{\mathrm{T}}+\boldsymbol{H}\boldsymbol{A}_Q\right)\left[\ddot{\boldsymbol{r}}_{\mathrm{b}}+\tilde{\dot{\omega}}\left(\boldsymbol{\rho}_{\mathrm{P}_0}+\boldsymbol{U}\right)+2\tilde{\omega}\underline{\dot{\boldsymbol{U}}}+\right.\right.$$
$$\left.\left.\tilde{\omega}\tilde{\omega}\left(\boldsymbol{\rho}_{\mathrm{P}_0}+\boldsymbol{U}\right)+\underline{\ddot{\boldsymbol{U}}}\right]\mathrm{d}\Omega+\boldsymbol{K}_0\boldsymbol{Q}\right\}=0,\tag{34}$$

where $\boldsymbol{H}=\boldsymbol{H}^{\mathrm{T}}$, and $\boldsymbol{\rho}_{\mathrm{P}_0}=\left[\ x_{\mathrm{P}}\quad 0\quad 0\ \right]^{\mathrm{T}}$. Eliminating the term $\delta\dot{\boldsymbol{Q}}^{\mathrm{T}}$ and then substituting $\boldsymbol{U}$, $\underline{\dot{\boldsymbol{U}}}$ and $\underline{\ddot{\boldsymbol{U}}}$ (Eqs. (20), (21) and (22)) into Eq. (34) becomes

$$\int_\Omega\rho\left(\boldsymbol{\Phi}^{\mathrm{T}}+\boldsymbol{H}\boldsymbol{A}_Q\right)\left\{\left(\boldsymbol{\Phi}+\boldsymbol{A}_Q^{\mathrm{T}}\boldsymbol{H}\right)\ddot{\boldsymbol{Q}}+2\tilde{\omega}\left(\boldsymbol{\Phi}+\boldsymbol{A}_Q^{\mathrm{T}}\boldsymbol{H}\right)\dot{\boldsymbol{Q}}+\right.$$
$$\left[\tilde{\dot{\omega}}\left(\boldsymbol{\Phi}+\frac{1}{2}\boldsymbol{A}_Q^{\mathrm{T}}\boldsymbol{H}\right)+\tilde{\omega}\tilde{\omega}\left(\boldsymbol{\Phi}+\frac{1}{2}\boldsymbol{A}_Q^{\mathrm{T}}\boldsymbol{H}\right)\right]\boldsymbol{Q}+$$
$$\left.\left(\ddot{\boldsymbol{r}}_{\mathrm{b}}+\tilde{\dot{\omega}}\boldsymbol{\rho}_{\mathrm{P}_0}+\tilde{\omega}\tilde{\omega}\boldsymbol{\rho}_{\mathrm{P}_0}+\dot{\boldsymbol{A}}_Q^{\mathrm{T}}\boldsymbol{H}\dot{\boldsymbol{Q}}\right)\right\}\mathrm{d}\Omega+\boldsymbol{K}_0\boldsymbol{Q}=0.\tag{35}$$

The above dynamic governing equation can be summarized as follows:

$$\boldsymbol{M}\ddot{\boldsymbol{Q}}+\boldsymbol{C}\dot{\boldsymbol{Q}}+\boldsymbol{K}\boldsymbol{Q}+\boldsymbol{F}=0.\tag{36}$$

In the linear dynamic model (L-model) for the beam, Eq. (36) is written as:

$$\boldsymbol{M}_{\mathrm{L}}\ddot{\boldsymbol{Q}}+\boldsymbol{C}_{\mathrm{L}}\dot{\boldsymbol{Q}}+\boldsymbol{K}_{\mathrm{L}}\boldsymbol{Q}+\boldsymbol{F}_{\mathrm{L}}=0.\tag{37}$$

In the proposed nonlinear coupling dynamic model (H-model), Eq. (36) is written as:

$$(\boldsymbol{M}_{\mathrm{L}}+\boldsymbol{M}_{\mathrm{H}})\ddot{\boldsymbol{Q}}+(\boldsymbol{C}_{\mathrm{L}}+\boldsymbol{C}_{\mathrm{H}})\dot{\boldsymbol{Q}}+(\boldsymbol{K}_{\mathrm{L}}+\boldsymbol{K}_{\mathrm{H}})\boldsymbol{Q}+$$
$$\boldsymbol{F}_{\mathrm{L}}+\boldsymbol{F}_{\mathrm{H}}=0,\tag{38}$$

where

Mass matrix:

$$\boldsymbol{M}\ddot{\boldsymbol{Q}}=\int_\Omega\rho\left(\boldsymbol{\Phi}^{\mathrm{T}}+\boldsymbol{H}\boldsymbol{A}_Q\right)\left(\boldsymbol{\Phi}+\boldsymbol{A}_Q^{\mathrm{T}}\boldsymbol{H}\right)\mathrm{d}\Omega\cdot\ddot{\boldsymbol{Q}};\tag{39}$$

$$\boldsymbol{M}_{\mathrm{L}}=\int_\Omega\rho\boldsymbol{\Phi}^{\mathrm{T}}\boldsymbol{\Phi}\mathrm{d}\Omega;\tag{40}$$

$$\boldsymbol{M}_{\mathrm{H}}=\int_\Omega\rho\boldsymbol{H}\boldsymbol{A}_Q\boldsymbol{\Phi}\mathrm{d}\Omega+\int_\Omega\rho\boldsymbol{\Phi}^{\mathrm{T}}\boldsymbol{A}_Q^{\mathrm{T}}\boldsymbol{H}\mathrm{d}\Omega+$$
$$\int_\Omega\rho\boldsymbol{H}\boldsymbol{A}_Q\boldsymbol{A}_Q^{\mathrm{T}}\boldsymbol{H}\mathrm{d}\Omega.\tag{41}$$

Damping matrix:

$$\boldsymbol{C}\dot{\boldsymbol{Q}}=\int_\Omega\rho\left(\boldsymbol{\Phi}^{\mathrm{T}}+\boldsymbol{H}\boldsymbol{A}_Q\right)\cdot 2\tilde{\omega}\cdot\left(\boldsymbol{\Phi}+\boldsymbol{A}_Q^{\mathrm{T}}\boldsymbol{H}\right)\mathrm{d}\Omega\cdot\dot{\boldsymbol{Q}};\tag{42}$$

$$\boldsymbol{C}_{\mathrm{L}}=2\int_\Omega\rho\boldsymbol{\Phi}^{\mathrm{T}}\tilde{\omega}\boldsymbol{\Phi}\mathrm{d}\Omega;\tag{43}$$

$$\boldsymbol{C}_{\mathrm{H}}=2\int_\Omega\rho\boldsymbol{\Phi}^{\mathrm{T}}\tilde{\omega}\boldsymbol{A}_Q^{\mathrm{T}}\boldsymbol{H}\mathrm{d}\Omega+2\int_\Omega\rho\boldsymbol{H}\boldsymbol{A}_Q\tilde{\omega}\boldsymbol{\Phi}\mathrm{d}\Omega+$$
$$2\int_\Omega\rho\boldsymbol{H}\boldsymbol{A}_Q\tilde{\omega}\boldsymbol{A}_Q^{\mathrm{T}}\boldsymbol{H}\mathrm{d}\Omega.\tag{44}$$

Stiffness matrix:

$$\boldsymbol{KQ} = \int_{\Omega} \rho \left(\boldsymbol{\Phi}^{\mathrm{T}} + \boldsymbol{HA_Q}\right) \left[\tilde{\omega}\left(\boldsymbol{\Phi} + \frac{1}{2}\boldsymbol{A}_{\boldsymbol{Q}}^{\mathrm{T}}\boldsymbol{H}\right) + \tilde{\omega}\tilde{\omega}\left(\boldsymbol{\Phi} + \frac{1}{2}\boldsymbol{A}_{\boldsymbol{Q}}^{\mathrm{T}}\boldsymbol{H}\right)\right] \mathrm{d}\Omega \cdot \boldsymbol{Q} + \int_{\Omega} \rho \left(\boldsymbol{HA_Q}\right)\left(\ddot{\boldsymbol{r}}_{\mathrm{b}} + \tilde{\dot{\omega}}\boldsymbol{\rho}_{\mathrm{P}_0} + \tilde{\omega}\tilde{\omega}\boldsymbol{\rho}_{\mathrm{P}_0}\right)\mathrm{d}\Omega + \boldsymbol{K}_0\boldsymbol{Q}; \tag{45}$$

$$\boldsymbol{K} = \boldsymbol{K}_{\mathrm{L}} + \boldsymbol{K}_{\mathrm{H}}; \tag{46}$$

$$\boldsymbol{K}_{\mathrm{L}} = \boldsymbol{K}_0 + \boldsymbol{K}_{\mathrm{f}}; \tag{47}$$

$$\boldsymbol{K}_{\mathrm{f}} = \int_{\Omega} \rho \boldsymbol{\Phi}^{\mathrm{T}} \tilde{\omega}\tilde{\omega}\boldsymbol{\Phi} \mathrm{d}\Omega + \int_{\Omega} \rho \boldsymbol{\Phi}^{\mathrm{T}} \tilde{\dot{\omega}}\boldsymbol{\Phi} \mathrm{d}\Omega; \tag{48}$$

$$\begin{aligned}\boldsymbol{K}_{\mathrm{H}} = &\frac{1}{2}\int_{\Omega} \rho \boldsymbol{\Phi}^{\mathrm{T}} \tilde{\dot{\omega}} A_{\boldsymbol{Q}}^{\mathrm{T}} \boldsymbol{H} \mathrm{d}\Omega + \int_{\Omega} \rho \boldsymbol{HA_Q} \tilde{\dot{\omega}} \boldsymbol{\Phi} \mathrm{d}\Omega + \\ &\frac{1}{2}\int_{\Omega} \rho \boldsymbol{HA_Q} \tilde{\dot{\omega}} A_{\boldsymbol{Q}}^{\mathrm{T}} \boldsymbol{H} \mathrm{d}\Omega + \int_{\Omega} \rho \boldsymbol{HA_Q} \tilde{\omega}\tilde{\omega} \boldsymbol{\Phi} \mathrm{d}\Omega + \\ &\frac{1}{2}\int_{\Omega} \rho \boldsymbol{\Phi}^{\mathrm{T}} \tilde{\omega}\tilde{\omega} A_{\boldsymbol{Q}}^{\mathrm{T}} \boldsymbol{H} \mathrm{d}\Omega + \frac{1}{2}\int_{\Omega} \rho \boldsymbol{HA_Q} \tilde{\omega}\tilde{\omega} A_{\boldsymbol{Q}}^{\mathrm{T}} \boldsymbol{H} \mathrm{d}\Omega + \\ &\int_{\Omega} \rho \left(\tilde{\dot{\omega}}\boldsymbol{\rho}_{\mathrm{P}_0}\right)_1 \boldsymbol{H} \mathrm{d}\Omega + \int_{\Omega} \rho \left[(\ddot{\boldsymbol{r}}_{\mathrm{b}})_1 + \left(\tilde{\omega}\tilde{\omega}\boldsymbol{\rho}_{\mathrm{P}_0}\right)_1\right] \boldsymbol{H} \mathrm{d}\Omega,\end{aligned} \tag{49}$$

where the symbol $()_1$ denotes the first element of a matrix.

Additional generalized force terms:

$$\boldsymbol{F}_{\mathrm{L}} = \int_{\Omega} \rho \boldsymbol{\Phi}^{\mathrm{T}} \ddot{\boldsymbol{r}}_{\mathrm{b}} \mathrm{d}\Omega + \int_{\Omega} \rho \boldsymbol{\Phi}^{\mathrm{T}} \tilde{\dot{\omega}} \boldsymbol{\rho}_{\mathrm{P}_0} \mathrm{d}\Omega + \int_{\Omega} \rho \boldsymbol{\Phi}^{\mathrm{T}} \tilde{\omega}\tilde{\omega} \boldsymbol{\rho}_{\mathrm{P}_0} \mathrm{d}\Omega; \tag{50}$$

$$\boldsymbol{F}_{\mathrm{H}} = \int_{\Omega} \rho \left(\boldsymbol{\Phi}^{\mathrm{T}} + \boldsymbol{HA_Q}\right) \dot{A}_{\boldsymbol{Q}}^{\mathrm{T}} \boldsymbol{H} \mathrm{d}\Omega \cdot \dot{\boldsymbol{Q}}, \tag{51}$$

where ~ notes a coordinate matrix of a vector, for example, $\tilde{\omega}$ is written as follows:

$$\tilde{\omega} = \begin{bmatrix} 0 & -\omega_3 & \omega_2 \\ \omega_3 & 0 & \omega_1 \\ -\omega_2 & \omega_1 & 0 \end{bmatrix} \tag{52}$$

As illustrated in Eqs. (37) and (38), the L-model is a linear model, but the H-model is a nonlinear higher-order model. And the H-model contains additional mass terms, damping terms, stiffness terms and additional generalized force than the L-model. All of these additional terms in the H-model are relevant to the higher-order geometrically nonlinear term H. Moreover, some of them are relevant to the coordinate matrix of the angular velocity $\tilde{\omega}$, the coordinate matrix of the angular acceleration $\tilde{\dot{\omega}}$ and the acceleration of the boundary $\ddot{\boldsymbol{r}}_{\mathrm{b}}$. In other words, the additional terms in the H-model are influenced by the motions of the body, which is more in accordance with the actual situation.

To simplify the following analysis, the angular acceleration term $\dot{\omega}$ and the acceleration of the foundation $\ddot{\boldsymbol{r}}_{\mathrm{b}}$ are neglected (these quantities are typically much smaller than the angular velocities). Moreover, because the rotational motion of the blades is mainly along one axis, the other components of the angular velocity (e.g., ω_1 and ω_2) are relatively small and are neglected to simplify the following analysis. Therefore, the stiffness terms $\boldsymbol{K}_{\mathrm{f}}$ and $\boldsymbol{K}_{\mathrm{H}}$ (some small higher-order quantities are neglected in $\boldsymbol{K}_{\mathrm{H}}$) are simplified as follows:

$$\boldsymbol{K}_{\mathrm{f}} = -\omega_3^2 \rho \cdot \int_{\Omega} \begin{bmatrix} \phi_x \phi_x^{\mathrm{T}} & 0 & 0 \\ 0 & \phi_y \phi_y^{\mathrm{T}} & 0 \\ 0 & 0 & 0 \end{bmatrix} \mathrm{d}\Omega; \tag{53}$$

$$\begin{aligned}\boldsymbol{K}_{\mathrm{H}} &\approx \int_{\Omega} \rho \begin{bmatrix} 0 & 0 & 0 \\ 0 & -\omega_3^2 x_{\mathrm{P}} H_y & 0 \\ 0 & 0 & -\omega_3^2 x_{\mathrm{P}} H_z \end{bmatrix} \mathrm{d}\Omega = \\ &\omega_3^2 \rho \int_{\Omega} x_{\mathrm{P}} \begin{bmatrix} 0 & 0 & 0 \\ 0 & \int_0^x \left(\frac{\partial \phi_y}{\partial x}\right) \cdot \left(\frac{\partial \phi_y}{\partial x}\right)^{\mathrm{T}} \mathrm{d}x & 0 \\ 0 & 0 & \int_0^x \left(\frac{\partial \phi_z}{\partial x}\right) \cdot \left(\frac{\partial \phi_z}{\partial x}\right)^{\mathrm{T}} \mathrm{d}x \end{bmatrix} \mathrm{d}\Omega.\end{aligned} \tag{54}$$

Eq. (53) shows that $\boldsymbol{K}_{\mathrm{f}}$ is negative and proportional to the square of the angular velocity. In other words, the stiffness of the flexible bodies in the L-model declines and the deformation is amplified with the rotational motion, which is inconsistent with the reality (Lee et al., 2001; Santos et al., 2004). In contrast, as shown in Eq. (54), $\boldsymbol{K}_{\mathrm{H}}$ is positive and increases with the square of the angular speed. In other words, the stiffness of the flexible bodies in the H-model increases with the rotational motion, which is more in line with the reality (Lee et al., 2001; Santos et al., 2004). The difference in the stiffness between the two modelling methods likely causes other differences in the dynamic behaviours in a rigid-flexible multi-body system. Moreover, as shown in Eq. (38), the H-model contains additional mass terms, damping terms, stiffness terms and generalized force terms. These additional terms likely also give rise to differences in the dynamic behaviour of a rigid-flexible coupled multi-body system between the two models. Detailed investigations and comparisons between the two modelling methods are conducted in the subsequent sections.

The aforementioned linear dynamic model and the nonlinear coupled dynamic model were both incorporated into our in-house aero-hydro-servo-elastic coupled FOWT simulation code DARwind to simulate the time-domain coupled dynamic behaviours of an FOWT system. In this section, the theories of the numerical program DARwind are briefly introduced.

(1) Aerodynamics (Hansen, 2015): The blade element momentum (BEM) method is used to calculate the aerodynamic loads. Several corrections are also considered, such as the Prandtl's blade-tip loss, hub-loss, the Glauert's correction, the skewed wake correction and the dynamic wake correction. The solution to the aerodynamic induction factors iterates until it converge to reasonable values.

(2) Hydrodynamics (Faltinsen, 1990; Newman, 1997): Airy linear wave theory, the potential flow theory and Morison's formula are applied to calculate the hydrodynamic loads. Hydrodynamic parameters are calculated by a preprocessor WAMIT. Subsequently, these frequency-domain hydrodynamic coefficients are taken as input data and con-

verted to the time-domain hydrodynamic loads in DARwind. Morison's formula is used to correct the flow-separation-induced nonlinear viscous drag on the floating platform.

(3) Mooring lines (Masciola et al., 2013): A quasi-static approach for a catenary mooring system is used in the code. The stretching of a mooring line is considered, but certain dynamic characteristics (e.g., the inertia, damping and bending) of the mooring system are neglected.

(4) Control system (Jonkman, 2007): Controller strategies consist of a generator-torque controller and a full-span rotor-collective blade-pitch controller. The generator-torque controller is mainly used to maximize the power capture below the rated wind speed. The blade-pitch controller is mainly used to regulate the generator speed and electrical power above the rated wind speed.

(5) Kinetics (Kane and Levinson, 1983; Huston and James, 1982): Kane's dynamic equations are used to establish the dynamic governing equations of an FOWT system. The adjacent array method is applied to describe the topological relation between the bodies of an FOWT system. The modal superposition method is applied to discretize the flexible bodies (e.g., blades and tower). The aforementioned linear dynamic model and the nonlinear coupled dynamic model are considered in the dynamic equations.

The code DARwind was developed using the above theories to model the time-domain coupled dynamic behaviours of an FOWT system. Compared with the other existing softwares, DARwind is more convenient to simulate FOWTs as different models. For example, the FOWT system can be modeled as a single rigid body system for less time cost, modeled as a multi-rigid-body system for a balance of the time cost and computational accuracy, or modeled as a rigid-flexible coupling multi-body system with or without considering nonlinear rigid-flexible coupled effects for accurate simulations but most time consuming. More details about the theories and verification of DARwind code can be found in Refs. (Hu et al., 2017; Chen et al., 2019).

3 Results and discussion

Tests (see Table 1) are conducted to compare differences between the H-model and L-model and to clarify the significance of the rigid-flexible coupling effects in an FOWT system. The floating platform is fixed to eliminate the influence from the 6-DOF motion of the floating platform for certain test cases (e.g., T1, T2, and T3). For the cases T4 and T6, the platform is moored by three catenary mooring lines. For T5, the floating platform moves in a specified manner regardless of external forces. The wave conditions are based on the JONSWAP wave spectrum with a significant wave height H_s, a peak period T_p, and a peak enhancement factor γ.

In the following tests, an OC4 semi-submersible FOWT (Robertson et al., 2014) is selected as the test object, in which the NREL-5MW reference wind turbine is used (Jonkman et al., 2009). Main properties of the OC4 semi-submersible FOWT are listed in Table 2. The construction of the OC4 semi-submersible FOWT are shown in Fig. 4. As shown in Fig. 4a, $O_0 - x_0y_0z_0$ is the global inertial frame and the origin O_0 is located at the intersection between the still water surface and the initial tower centreline. $O_1 - x_1y_1z_1$ is the body-fixed frame of the floating platform, which initially coincides with the frame of global inertial frame. $O_b - x_by_bz_b$ is the local body-fixed frame of each blade, fixed at the blade root (see Fig. 4b). The positive direction of the x_b-axis points to the nacelle and the z_b-axis is along the neutral axis of the blade, which is different from Fig. 2.

3.1 Dynamic stiffening effect and influencing factors

This subsection investigates the relationship between the rotational speed and bending stiffness of the blades for the two models (L-model and H-model). Calculations are conducted for the test case T1 (see Table 1). In T1, the supporting platform is fixed, and the rotor rotates at different rotational speeds without suffering from aerodynamic loads. The first natural frequencies of the blades in flapwise and edgewise modes under different rotational speeds are listed in Table 3 and plotted in Fig. 5. The results are compared with those calculated by FAST (Jonkman et al., 2005; Jonkman, 2007). Table 3 and Fig. 5 show that the results calculated by Darwind (H-model) and FAST are in good consistency. More comparisons on the dynamic responses between these two codes can be found in the reference (Hu et al., 2017).

Comparing the results calculated by the H-model and L-model (see Table 3 and Fig. 5), we know that the flapwise natural frequency of the L-model's blades is nearly con-

Table 1 Test case matrix

Test case	Platform state	V_{wind} (m/s)	Wave condition	Ω (rmp)	BtDef (m)
T1	Fixed	0.00	Still water	0–30	0.0
T2	Fixed	11.4	Still water	12.1	0.0
T3	Fixed	11.4	Still water	20.0	0.0
T4	Moored	0.00	Still water	0.00	4.0
T5	Specified	0.00	Still water	0.00	1.0
T6	Moored	11.4	Irregular wave	12.1	0.0

Notes: "V_{wind}" represents the steady wind speed; "Ω" represents the rotor speed; "BtDef" denotes the initial deformation at the blade tips. Irregular wave condition: H_s=2 m, T_p=8 s, γ=3.3.

stant under different rotational speed conditions and the edgewise frequency in the L-model declines with the rotational speed. It is consistent with Eq. (53) in that the out-of-plane (flapwise) stiffness of the L-model is not influenced by the rotational speed, but the in-plane (edgewise) stiffness declines and is even negative when the rotational speed exceeds its fundamental natural frequency. In contrast, in the H-model, the natural frequency of the blades increases with the rotational speed in both the flapwise and edgewise modes. In other words, the stiffness of the H-model's blades increases with the rotational speed, which is in accordance with Eq. (54). Relevant experiments (Lee et al., 2001; Santos et al., 2004) have also proved that flexible bodies stiffen when undergoing large rotational motions and the stiffening effects increase with the rotational speed, which is the so called "dynamic stiffening effect" (Liu and Hong, 2003). On the other hand, Cai et al.(2005) found that a numerical divergence might appear using the linear dynamic model (L-model) when the rotational speed of the flexible beam is close to or exceeds its fundamental natural frequency. Fortunately, the operating rotational speed of the wind turbine blades is generally much smaller than the fundamental natural frequency.

The above analysis demonstrates that the stiffness of the blades in the H-model and L-model are different, and the gap even increases with the blades rotational speed. The differences likely introduce dynamic differences between the two models, e.g., aerodynamic loads, structural loads and blade deflection. Thus, the test case T2 (see Table 1) was

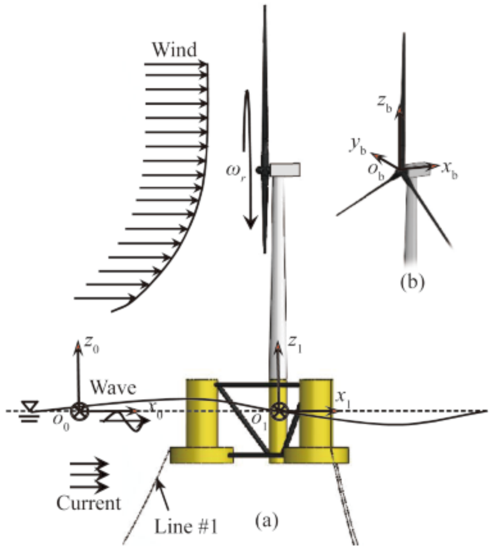

Fig. 4. Overview of an OC4 semi-submersible FOWT.

Table 2 Main properties of an OC4 semi-submersible FOWT

Property	Values
Rated power	5 MW
Rated wind & rotor speed	11.4 m/s, 12.1 rpm
Rotor type	Upwind, 3 blades
Rotor diameter	126 m
Tower height	77.6 m
Platform type	Semisubmersible
Water depth	200 m
Mooring system	3 lines, catenary

Table 3 First natural frequency of the blades in the two models

Rotor speed (rad/s)	Flapwise (*x*) (rad/s)			Edgewise (*y*) (rad/s)		
	FAST	Darwind		FAST	Darwind	
		H	L		H	L
0.000	4.41577	4.43970	4.41896	6.80595	6.89014	6.89014
0.722	4.50996	4.52327	4.41896	6.84829	6.91088	6.84804
0.942	4.56353	4.58610	4.41896	6.84836	6.91088	6.82731
1.267	4.70993	4.73312	4.41896	6.86878	6.93161	6.76448
2.094	5.21296	5.23515	4.41896	6.95278	7.01580	6.55462
3.140	6.06013	6.09406	4.41896	7.12011	7.20430	6.13616

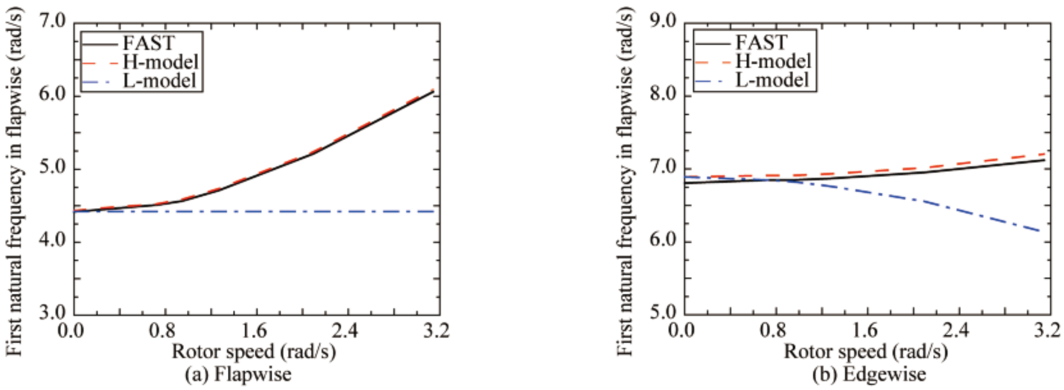

Fig. 5. First natural frequency of the blades in the two models.

conducted to compare the dynamic responses between the two models, and the test results are listed in Table 4. Comparing the results calculated by the H-model and the L-model (see Table 4), we know that the lateral blade-tip deformations in the H-model are smaller than those in the L-model. In addition, there is an axial foreshortening displacement in the H-model but that keeps zero in the L-model. For the structural loads at the blade root, the mean shear force and bending moment of the H-model is slightly smaller than those of the L-model. However, the standard deviation of the structural loads on the H-model is slightly larger than that of the L-model. In other words, the H-model has smaller structural loads but more variation of the structural loads at the blade root. For the aerodynamic loads, not only the aerodynamic thrust force but also the aerodynamic torque of the H-model are slightly smaller than those of the L-model.

Table 4 Comparison of the deformation and aerodynamic loads from the two models

	Model	Mean	St. Dev.
BtDefx (m)	H	5.629	0.166
	L	6.641	0.167
BtDefy (m)	H	0.221	0.319
	L	0.232	0.334
BtDefz (m)	H	–0.438	0.023
	L	0.000	0.000
Fxbrt (kN)	H	–247.429	4.369
	L	–248.135	4.075
Mybrt (kN·m)	H	–10121.600	195.010
	L	–10159.000	182.178
RotThrust (kN)	H	736.383	9.308
	L	738.411	9.917
RotTorque (kN·m)	H	4310.453	92.685
	L	4317.001	97.528

Notes: "BtDefx" and "BtDefy" represent the blade-tip lateral displacement along the x_b-axis and the y_b-axis, respectively; "BtDefz" represents the blade-tip foreshortening displacement along the z_b-axis; "Fxbrt" represents the shear force at a blade root along the x_b-axis; "Mybrt" represents the bending moment at a blade root along the y_b-axis; "RotThrust" represents the aerodynamic thrust force on the rotor; "RotTorque" represents the aerodynamic torque on the rotor.

The deformation along a blade for the test case T2 (12.1 rpm, see Table 1) and T3 (20.0 rpm, see Table 1) obtained from the two models is compared in Fig. 6, which shows that the deflection along the blade in the H-model is generally smaller than that in the L-model, and the gap increases with the rotor speed. In addition, the colour variation along a blade is nonlinear. Deformation in the first half of the blades changes slowly, whereas that in the last half of the blades changes more rapidly. The above analysis demonstrates that the blade stiffness in the H-model is larger than that in the L-model and that the difference increases with the rotor speed. Finally, the larger stiffness gives rise to smaller deformation.

The differences observed in the aerodynamic loads and structural loads at the blade root (see Table 4) between the

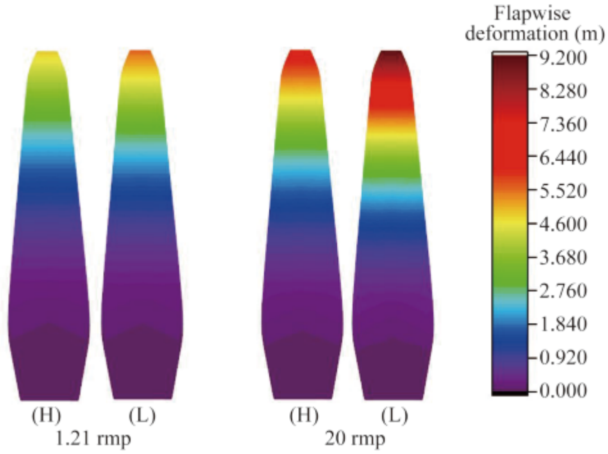

Fig. 6. Comparison of deformation along a blade from two models.

two models are due to the differences of the deflection of the blades between the two models. The lateral displacements of the blades in the H-model are smaller than those in the L-model due to the "dynamic stiffening" effect (Liu and Hong, 2004) in the H-model. In contrast, the axial deformation of the L-model is zero, whereas that of the H-model is negative. This is the effect of the "foreshortening displacement" caused by the nonlinear coupling effect from the lateral displacements, as shown in Eq. (11). Hence, the total arc length of the rotating blade in the H-model (S_H in Fig. 7) is smaller than that in the L-model (S_L in Fig. 7). The blades with a shorter arc length and effective vertical length, hence have less effective windward area, and are subjected to the smaller aerodynamic loads and structural loads at the blade root. In addition, the overvalued deflection predicted by the L-model also cause inaccuracy in the aerodynamic algorithm with the increasing rotational speed.

3.2 Interaction between the blades and the supporting platform

Research shows that there are complicated interactive effects in a rigid-flexible multi-body system undergoing

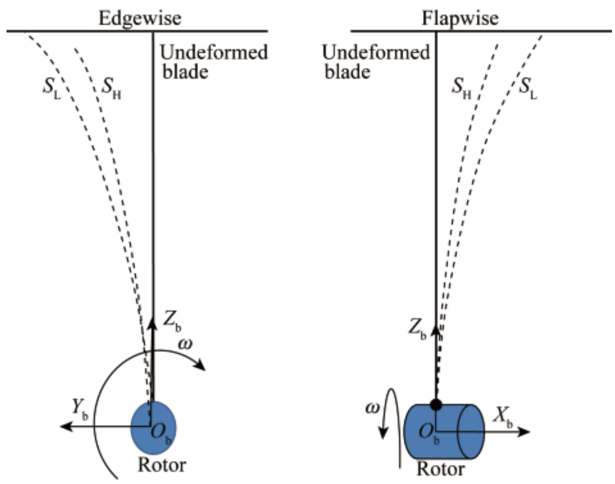

Fig. 7. Illustration of the blade deformation between models.

large overall motions (Cai et al., 2005; Liu and Hong, 2003). Hence, the interactive effects from the flexible blades and the motions of the floating platform of an FOWT system are investigated and compared between the H-model and L-model in this section.

In the example of test T4 (see Table 1), the floating platform is moored by a catenary mooring system in still water. Additionally, one of the blades vibrates with an initial out-of-plane blade-tip displacement of 4 m. The calculation results of the floating supporting platform motion (surge, heave, pitch and yaw) between the models are shown in Fig. 8. These figures indicate that the vibration of the flexible blades gives rise to small high-frequency fluctuations in the platform motions. The fluctuation in the H-model is typically larger than that in the L-model in general. In addition, it is interesting that vibration of the blades in the H-model causes a slight offset of the mean position of the floating supporting platform.

When the floating platform decays with an initial displacement of 0.5° in the pitch, the vibration of the blades also gives rise to some small high-frequency fluctuations of the platform motions as shown in Fig. 9. Furthermore, the flexible bodies even change the natural period of the pitch motion of an FOWT system, which was also found by Matha et al. (2010).

Several studies (Mayo et al., 1995; Liu and Hong, 2004) have also proven that not only the angular motions but also the translational motions of the rigid bodies can affect the dynamic behavior of the flexible bodies. In this subsection, a test is performed for the case T5 (see Table 1). In the test, the heave motion of the floating platform is specified with an initial blade-tip deformation of 1 m as follows:

$$\ddot{\xi} = -A_{\rm m}\omega^2 \sin(\omega t), \quad (55)$$

where $\ddot{\xi}$ is the acceleration of the heave motion, $A_{\rm m} = 3$ m, and ω is the heave motion frequency, which takes values of 0.16 rad/s and 16 rad/s, respectively.

Fig. 10 shows that the vibration amplitude of the blades increases with the heave motion frequency (0.16 rad/s to 16 rad/s), due to the increased generalized force terms in Eq. (50). For example, the term $\int_\Omega \rho \boldsymbol{\Phi}^{\rm T} \ddot{\boldsymbol{r}}_{\rm b} {\rm d}\Omega$ in Eq. (50) is influenced by the motions of the floating platform. Moreover, compared with the vibration curve of the blade in the L-model (dashed line in Fig. 10), the vibration curve in the H-model (solid line in Fig. 10) offsets slightly, and this trend intensifies with the motion frequency. This occurs because the natural frequencies of the blades in the H-model are affected by the motions of the floating platform. As shown in Eq. (49), the term $\int_\Omega \rho (\ddot{\boldsymbol{r}}_{\rm b})_1 \boldsymbol{H} {\rm d}\Omega$ in Eq. (49) affects the natural frequencies of the blades to a small extent due to the movement of the floating supporting platform $\ddot{\boldsymbol{r}}_{\rm b}$.

In conclusion, compared with the rigid-bodies model, there are interactive effects between the flexible bodies and the 6-DOF motions of the floating supporting platform in an FOWT system. These coupling effects in the H-model are more distinct than those in the L-model.

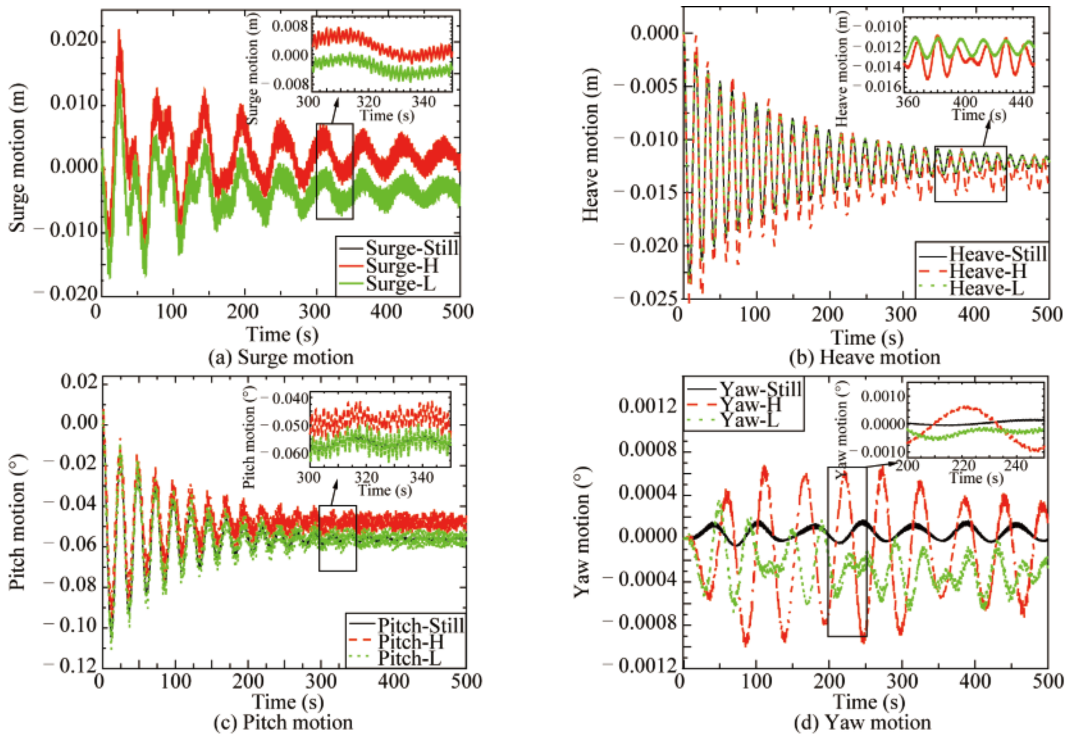

Fig. 8. Illustration of the blade deformation between the models. ("-still" represents an FOWT in still water without the blades vibration; "-H" represents a nonlinear model with the blades vibration; "-L" represents a linear model with the blades vibration)

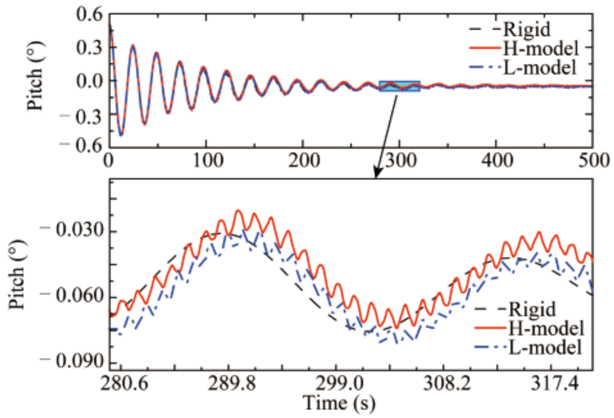

Fig. 9. Pitch decay for the rigid-bodies model, H-model and L-model.

3.3 Comparison of the global dynamic responses

The above analysis demonstrates that large overall motions (e.g., rotor rotation and 6-DOF motions of the floating platform) can affect dynamic responses of the flexible blades, vice versa, the flexible bodies affect the motion of the system as well. In addition, there are differences in the coupling effects between the H-model and L-model. Hence, under operational conditions, the global dynamic responses (e.g., 6-DOF motions, mooring line tension, aerodynamic loads) of the FOWT might also be different between the two models. In this subsection, a combined wind/wave case T6 (see Table 1) is conducted to compare the global dynamic responses of the two models.

The statistical data of the H-model and L-model for T6 are compared in Table 5. The load case T6 is simulated for the duration of 3600 s (time step is 0.0125 s) and the statistical data are calculated based on the time-series data by the statistical tool OriginPro. The extreme values include the minimum and maximum of the time-series data. Table 5 shows that the mean value, standard deviation (St. Dev.) and extreme values of the dynamic responses (aerodynamic loads, structural loads at the blade root, surge motion, pitch

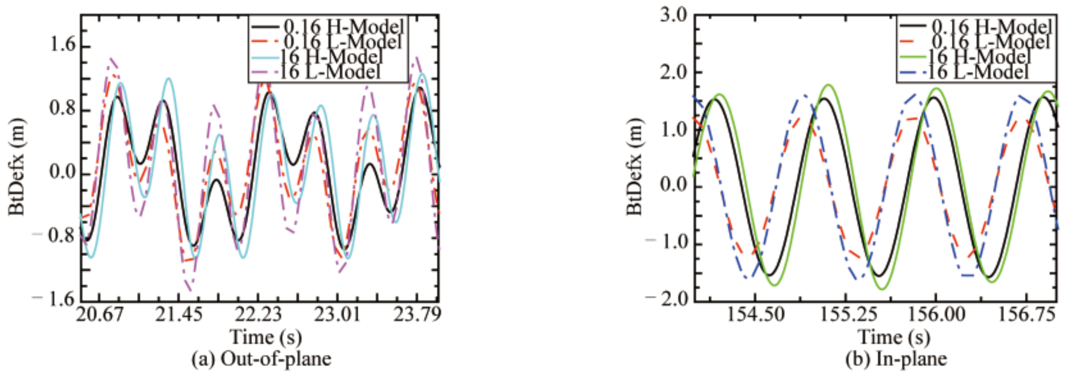

Fig. 10. Blade-tip displacements of the two models (heave motion frequency of 0.16 rad/s to 16 rad/s).

Table 5 Comparison of the global dynamic responses between the two models

Item	Model	Mean	St. Dev.	Minimum	Maximum
RotThrust (kN)	H	725.661	34.956	395.296	834.822
	L	727.576	35.319	390.046	838.025
RotTorque (kN·m)	H	4189.843	408.280	1206.827	5617.833
	L	4195.145	410.475	1176.642	5590.204
Fxbrt (kN)	H	–247.501	8.141	–275.981	–136.249
	L	–248.224	7.804	–276.973	–134.942
Mybrt (kN·m)	H	–10135.600	327.648	–11229.200	–4900.450
	L	–10174.000	311.640	–11275.700	–4831.470
Surge (m)	H	1.761	0.275	–0.052	2.503
	L	1.766	0.275	–0.054	2.507
Pitch (°)	H	3.029	0.407	–0.039	4.712
	L	3.040	0.409	–0.041	4.724
FairlTen (kN)	H	2889.250	71.508	2502.982	3127.838
	L	2890.356	71.644	2502.661	3129.013
BtDefx (m)	H	5.613	0.285	0.000	6.565
	L	6.621	0.319	0.000	7.633
BtDefy (m)	H	0.215	0.316	–0.302	0.747
	L	0.225	0.331	–0.319	0.782
BtDefz (m)	H	–0.436	0.043	–0.595	0.000
	L	0.000	0.000	0.000	0.000

Notes: "FairlTen" represents the tension force of the fairlead.

motion, mooring lines tension and blade deflection) of the H-model are smaller than those of the L-model in general. As noted above, there are differences in the blade stiffness and blade deformation between the two models. These differences result in larger aerodynamic loads and structural loads in the L-model. Consequently, the larger aerodynamic loads in the L-model cause the corresponding larger 6-DOF motions and mooring line tension forces. In other words, the extreme values in an FOWT system could be overestimated when using the L-model.

4 Conclusions

In this paper, a nonlinear rigid-flexible coupling dynamic model is proposed to simulate dynamic behaviors of floating wind turbines. Subsequently, a series of testing cases are conducted to investigate the rigid-flexible coupling effects of an FOWT system and compare the differences between the linear dynamic model and the proposed nonlinear coupled dynamic model.

Conclusions are summarized as: Firstly, the coupling axial displacements caused by the lateral displacements play an important role in a rigid-flexible coupled multi-bodies FOWT system with larger overall motions, which is also the essential difference between the linear dynamic model and the proposed nonlinear coupled dynamic model. Secondly, a series of tests demonstrate that the lateral stiffness of the blades in the linear dynamic model declines (or holds constant) with the increase of the rotational speed of the rotor, but that in the nonlinear coupled dynamic model increases with the increase of the rotational speed of the rotor, which is more in line with the actual situation. Thirdly, the interactive effects between the flexible bodies (e.g., blades) and the motions of rigid bodies (e.g., the floating supporting platform) in the nonlinear coupled dynamic model are more distinct than those in the linear dynamic model. Fourthly, the aerodynamic loads, blades deformation and global dynamic responses in the linear dynamic model are slightly larger than those in the nonlinear coupled dynamic model. In other words, extreme values could be overestimated using the linear dynamic model. In general, the rigid-flexible coupling effects in floating offshore wind turbines should be paid attention to and the nonlinear coupled dynamic model is more appropriate than the linear dynamic model in general.

Acknowledgements

This work was supported by the State Key Lab of Ocean Engineering, Shanghai Jiao Tong University, and all of these supports are gratefully acknowledged by the authors.

References

Andreaus, U., Baragatti, P. and Placidi, L., 2016. Experimental and numerical investigations of the responses of a cantilever beam possibly contacting a deformable and dissipative obstacle under harmonic excitation, *International Journal of Non-Linear Mechanics*, 80, 96–106.

Bachynski, E.E. and Moan, T., 2012. Design considerations for tension leg platform wind turbines, *Marine Structures*, 29(1), 89–114.

Banerjee, A.K. and Dickens, J.M., 1990. Dynamics of an arbitrary flexible body in large rotation and translation, *Journal of Guidance*, *Control*, *and Dynamics*, 13(2), 221–227.

Bauchau, O.A., 2011. *Flexible Multibody Dynamics*, Springer, New York, 752.

Cai, G.P., Hong, J.Z. and Yang, S.X., 2005. Dynamic analysis of a flexible hub-beam system with tip mass, *Mechanics Research Communications*, 32(2), 173–190.

Chen, J., Hu, Z., Liu, G. and Wan, D., 2019. Coupled aero-hydro-servo-elastic methods for floating wind turbines, *Renewable Energy*, 130, 139–153.

Faltinsen, O.M., 1990. *Sea Loads on Ships and Offshore Structures*, Cambridge University Press, Cambridge, New York.

Hansen, M.O.L., 2015. *Aerodynamics of Wind Turbines*, Routledge, London, New York.

Held, A., Nowakowski, C., Moghadasi, A., Seifried, R. and Eberhard, P., 2016. On the influence of model reduction techniques in topology optimization of flexible multibody systems using the floating frame of reference approach, *Structural and Multidisciplinary Optimization*, 53(1), 67–80.

Hu, Z.Q., Chen, J.H. and Liu, G.L., 2017. Investigation on high-order coupled rigid-flexible multi-body dynamic code for offshore floating wind turbines, *Proceedings of the 36th International Conference on Ocean*, *Offshore and Arctic Engineering*, ASEM, Trondheim, Norway.

Huston, R.L. and Kamman, J.W., 1982. A discussion on constraint equations in multibody dynamics, *Mechanics Research Communications*, 9(4), 251–256.

Jonkman, J., Butterfield, S., Musial, W. and Scott, G., 2009. *Definition of a 5-MW Reference Wind Turbine for Offshore System Development*, National Renewable Energy Laboratory, Golden, CO.

Jonkman, J.M., 2007. *Dynamics Modeling and Loads Analysis of an Offshore Floating Wind Turbine*, National Renewable Energy Laboratory, Golden, CO.

Jonkman, J.M. and Buhl Jr., M.L., 2005. *FAST User's Guide-Updated August 2005*, NREL/TP-500–38230, National Renewable Energy Laboratory (NREL), Golden, CO.

Jourdain, P.E.B., 1909. Note on an analogue of Gauss' principle of least constraint, *The Quarterly Journal of Pure and Applied Mathematics*, 8, 153–157.

Kane, T.R. and Levinson, D.A., 1983. The use of Kane's dynamical equations in robotics, *The International Journal of Robotics Research*, 2(3), 3–21.

Kane, T.R., Ryan, R.R. and Banerjee, A.K., 1989. Dynamics of a cantilever beam attached to a moving base, *Journal of Guidance*, *Control*, *and Dynamics*, 10(2), 139–151.

Karimirad, M., Meissonnier, Q., Gao, Z. and Moan, T., 2011. Hydroelastic code-to-code comparison for a tension leg spar-type floating wind turbine, *Marine Structures*, 24(4), 412–435.

Larsen, J.W. and Nielsen, S.R.K., 2006. Non-linear dynamics of wind turbine wings, *International Journal of Non-Linear Mechanics*, 41(5), 629–643.

Lee, C.L., Al-Salem, M.F. and Woehrle, T.G., 2001. Natural frequency measurements for rotating spanwise uniform cantilever beams, *Journal of Sound and Vibration*, 240(5), 957–961.

Lee, D., Hodges, D.H. and Patil, M.J., 2002. Multi-flexible-body dynamic analysis of horizontal axis wind turbines, *Wind Energy*, 5(4), 281–300.

Likins, P.W., 1972. Finite element appendage equations for hybrid coordinate dynamic analysis, *International Journal of Solids and Structures*, 8(5), 709–731.

Liu, A.Q. and Liew, K.M., 1994. Non-linear substructure approach for dynamic analysis of rigid-flexible multibody systems, *Computer Methods in Applied Mechanics and Engineering*, 114(3–4), 379–396.

Liu, J.Y. and Hong, J.Z., 2003. Geometric stiffening of flexible link system with large overall motion, *Computers & Structures*, 81(32), 2829–2841.

Liu, J.Y. and Hong, J.Z., 2004. Geometric stiffening effect on rigid-flexible coupling dynamics of an elastic beam, *Journal of Sound and Vibration*, 278(4–5), 1147–1162.

Ma, Y., Hu, Z.Q. and Xiao, L.F., 2015. Wind-wave induced dynamic response analysis for motions and mooring loads of a spar-type offshore floating wind turbine, *Journal of Hydrodynamics*, *Ser. B*, 26(6), 865–874.

Marshall, B., 2002. *NWTC Information Portal*, https://nwtc.nrel.gov/Modes [2014-09-28].

Masciola, M., Jonkman, J. and Robertson, A., 2013. Implementation of a multisegmented, quasi-static cable model, *Proceedings of the 23rd International Offshore and Polar Engineering Conference*, International Society of Offshore and Polar Engineers, Alaska, USA.

Matha, D., Fischer, T., Kuhn, M. and Jonkman, J., 2010. *Model Development and Loads Analysis of a Wind Turbine on a Floating Offshore Tension Leg Platform*, National Renewable Energy Laboratory, Golden, Colorado.

Mayo, J., Dominguez, J. and Shabana, A.A., 1995. Geometrically nonlinear formulations of beams in flexible multibody dynamics, *Journal of Vibration and Acoustics*, 117(4), 501–509.

Nada, A.A., Hussein, B.A., Megahed, S.M. and Shabana, A.A., 2010. Use of the floating frame of reference formulation in large deformation analysis: Experimental and numerical validation, *Proceedings of the Institution of Mechanical Engineers*, *Part K*: *Journal of Multibody Dynamics*, 224(1), 45–58.

Namik, H. and Stol, K., 2010. Individual blade pitch control of floating offshore wind turbines, *Wind Energy*, 13(1), 74–85.

Nejad, A.R., Bachynski, E.E., Kvittem, M.I., Luan, C.Y., Gao, Z. and Moan, T., 2015. Stochastic dynamic load effect and fatigue damage analysis of drivetrains in land-based and TLP, spar and semi-submersible floating wind turbines, *Marine Structures*, 42, 137–153.

Newman, J.N., 1997. *Marine Hydrodynamics*, The MIT Press, Cambridge, Massachusetts, USA.

Nowakowski, C., Fehr, J., Fischer, M. and Eberhard, P., 2012. Model order reduction in elastic multibody systems using the floating frame of reference formulation, *IFAC Proceedings Volumes*, 45(2), 40–48.

Øye, S., 1996. FLEX4 simulation of wind turbine dynamics, *Proceedings of the 28th IEA Meeting of Experts Concerning State of the Art of Aeroelastic Codes for Wind Turbine Calculations*, Technical University of Denmark, Lyngby.

Pérez-Collazo, C., Greaves, D. and Iglesias, G., 2015. A review of combined wave and offshore wind energy, *Renewable and Sustainable Energy Reviews*, 42, 141–153.

Robertson, A., Jonkman, J., Masciola, M., Song, H., Goupee, A., Coulling, A. and Luan, C., 2014. *Definition of the Semisubmersible Floating System for Phase II of OC4*, National Renewable Energy Laboratory, Golden, CO.

Santos, I.F., Saracho, C.M., Smith, J.T. and Eiland, J., 2004. Contribution to experimental validation of linear and non-linear dynamic models for representing rotor-blade parametric coupled vibrations, *Journal of Sound and Vibration*, 271(3–5), 883–904.

Shabana, A.A., 1997. Flexible multibody dynamics: Review of past and recent developments, *Multibody System Dynamics*, 1(2), 189–222.

Sharf, I., 1995. Geometric stiffening in multibody dynamics formulations, *Journal of Guidance*, *Control*, *and Dynamics*, 18(4), 882–890.

Wang, L. and Sweetman, B., 2013. Multibody dynamics of floating wind turbines with large-amplitude motion, *Applied Ocean Research*, 43, 1–10.

Wang, L.S. and Pao, Y.H., 2003. Jourdain's variational equation and Appell's equation of motion for nonholonomic dynamical systems, *American Journal of Physics*, 71(1), 72–82.

Winfrey, R.C., 1971. Elastic link mechanism dynamics, *Journal of Engineering for Industry*, 93(1), 268–272.